Proceedings of the ASME 2011 5th International Conference on Energy Sustainability & 9th Fuel Cell Science, Engineering and Technology Conference
ESFuelCell2011
August 7-10, 2011, Washington, DC, USA

ESFuelCell2011-54153

PROJECTION OF FLAT-PLANE FLUXMAP IMAGES ONTO NON-FLAT RECEIVER SURFACES

Julius Yellowhair
Charles E. Andraka
Sandia National Laboratories
National Solar Thermal Test Facility
P. O. Box 5800, MS 1127
Albuquerque, NM 87185-1127, USA

ABSTRACT

When designing or evaluating a dish concentrator system, it is desirable to determine the incident flux profile on the receiver surface, regardless of the absorber surface geometry. During the design process, analytical tools are used to predict flux profiles. During product evaluation, a flux-mapper (beam characterization system) can be used to measure the flux profile on a flat target surface.

Radiosity concerns typically limit flux mapping measurements of dish-engine systems to a flat plate target. We propose and demonstrate an analytical method to project such a measured flat-target flux profile onto a non-flat receiver surface. We analytically estimate the angular content of the flux profile, and use this estimate combined with the measured flat-plate flux profile to project an estimate of the flux pattern onto another receiver surface.

In this paper, we analytically demonstrate the technique. We first model a dish concentrator using CIRCE2. We then develop an analytic flux-map, in CIRCE2, on a flat target, simulating a flux-mapper output. Next, we use our new software tool and the CIRCE2 angular flux binning to project this flux pattern onto a non-flat receiver surface. Finally, we run a CIRCE2 model of the same dish with the non-flat target geometry, and compare this CIRCE2 output to the projected data. We also demonstrate the technique using a measured flux-map from a dish system in the field.

1. INTRODUCTION

Dish concentrators can produce highly concentrated flux for the operation of an engine. A variety of system error sources can contribute to non-ideal flux distributions on the receiver [1]. It then becomes important to evaluate the flux distributions on the receiver. Knowledge from the flux distribution can be used to relieve any hot spots, for example, through alignment corrections. This knowledge can also be used to evaluate impacts on performance and life, and to determine the acceptability of the flux distribution. However, radiosity concerns (i.e. due to reflection and re-emission of flux from the surfaces) limit flux mapping measurements of dish systems to a flat plate target. Sections of real receivers are typically conical or spherical where heat-absorbing coils or surfaces are located. It is the flux on these non-flat receiver geometries that needs evaluations, but flux-maps on these non-flat surfaces are not easily obtained directly. In the past, to estimate the flux distribution on real receivers, multiple flux maps on flat targets along the dish axis were acquired. The measurements were typically closely spaced in the region of the non-flat receiver section (i.e. slicing the non-flat receiver with flat plate measurements). The flux on the flat plates were then analytically mapped to the non-flat surface of the receiver at the intersections and interpolated everywhere else. The limitation with this method is that the angular content of the flux intensities are ignored and not conserved, and so the flux is not properly mapped onto the non-flat surface. This method can hide or accentuate problem areas in the flux distribution on the non-flat receiver.

In this paper, we propose and demonstrate a method to project such a measured flat-target flux profile onto a non-flat receiver surface [2]. We analytically estimate the angular content of the design flux profile, and use this estimate combined with the measured flat-plate flux profile to project an estimate of the flux pattern onto another receiver surface geometry.

To develop the method we use CIRCE2 [3] to estimate the design flux profiles of a dish concentrator on a flat plate located between the focal plane and the receiver surface. CIRCE2 is a

computer code developed by Sandia National Laboratories for modeling the optical performance of solar concentrators and evaluating the reflected flux distributions at the receiver or target. An added feature of CIRCE2 bins the reflected flux at the target plane into elemental solid angles [4]. We use this flux angular binning feature to estimate the intensity contained in each elemental solid angle of the propagating flux. We model the design case, and assume that, with "reasonable" error content, the relative angular content remains fixed. We then use this angular information from a model of the dish system to project the measured flux profile to other planes or surfaces (e.g. conical and spherical) at different locations along the dish optical axis.

In this paper, we analytically demonstrate the technique. We model a dish concentrator in CIRCE2. We then develop an analytic flux-map on a flat target. Next, we use our new software tool, and the CIRCE2 angular flux binning, to project this flux pattern onto a non-flat receiver surface. Finally, we run a CIRCE2 model of the same dish with the non-flat target geometry, and compare this CIRCE2 output to the projected data. We also demonstrate the technique using a measured fluxmap from a dish system in the field.

2. APPROACH

2.1. CIRCE2 Flux Angle Binning

The subject dish system is modeled in CIRCE2 to determine the profile of the reflected flux on a flat target plane. In our CIRCE2 model the flat target plate is placed between the focal plane of the dish and the receiver surface. With the flux angular binning feature of CIRCE2 turned on, the incident flux on the flat target plate is subdivided into solid angle bins for each cell (or pixel) of flux data at the target plate. There are a few options for angular binning that the user can specify such as the angular bin size, the polar (θ) angular range to which the solid angles will be binned, target grid size, and number of grid points or cells. The number of angular bins determines the angular bin size. A large number of angular bins (i.e. small angular bin size) and grid points samples the incident flux at the flat plate at a high resolution but at the expense of longer processing times. At the maximum sampling resolution, processing times can approach tens of minutes, whereas for a lower to moderate sampling resolution the processing times is typically a few minutes.

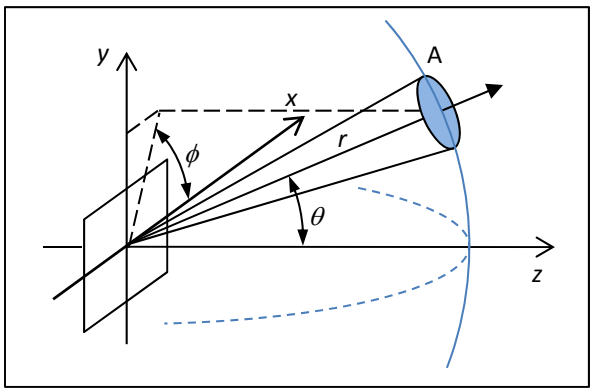

Fig. 1. Illustration of a solid angle. The area, A, on a sphere at radius, r, subtends a solid angle of A/r^2 steradians. When the flux is angular binned, the area A carries the binned intensity.

Figure 1 shows an illustration of a single circular solid angle bin with the coordinates and angles defined. In CIRCE2 the size of the solid angle bin is governed by the differential size of polar and azimuthal angles, $\Delta\theta$ and $\Delta\phi$, respectively. The azimuthal (ϕ) space ranges from 0 to 2π radians (0 - 360°) and can be divided up to 90 (max setting) equally spaced angle sectors (i.e. $\Delta\phi_{min} = 2\pi/90$). Similarly, the polar angle (θ) space ranges from 0 and up to $\pi/2$ radians (90°) and can be divided up to 45 (max setting) equally spaced angle sectors. For the results reported in this paper, we limited the polar angle range from 0 to $\pi/3$ radians (0 - 60°). This partitioning procedure results in a set of ordinates defined by the intersections of the polar and azimuthal angle segments. The result is an angle bin that is trapezoidal in shape as shown in Figure 4. The number of elemental solid angle bins generated per cell is then given by

$$N_{\text{bins}} \le \frac{\pi}{2\Delta\theta} \times \frac{2\pi}{\Delta\phi}. \qquad (1)$$

The direction of the propagating flux is determined by following the reflected flux at the concentrator facet, or subfacet, to the incident point on the target element. This flux is assigned to the angle bin that points in the same direction. This process is repeated for all the angular bins at all the cells.

The flux density, or irradiance, incident on a single target cell must be conserved. The irradiance, E_k (W/m^2), is incident on the cell k from the concentrator side. Power (W) on the k^{th} cell is obtained from the irradiance by

$$\Phi_k = E_k A_k, \qquad (2)$$

where A_k is the area of the cell.

The power at the cell is then subdivided into solid angles to get the intensities, I (W/sr), in each solid angle bin,

$$I_{ki} = \frac{\mathrm{d}\Phi_k}{\mathrm{d}\omega_i}, \qquad (3)$$

where $\mathrm{d}\omega_i$ is the i^{th} elemental solid angle within a cell and I_{ki} is the intensity binned into the i^{th} solid angle of the k^{th} cell. The parameter i ranges from 1 to N_{bins}. Figure 2 schematically illustrates the flux incident on a 3 × 3 target cell array and the directions of the solid angles after binning. That is, the incident flux is sampled at each cell and then angularly binned within the cells. For the conservation of energy to hold (i.e. the energy incident on the cell k), we calculate the irradiance at some distance, r, from the cell by,

$$E_k^{'} = \frac{\sum_i \Phi_{ki}}{A_{\text{sph}}} \approx E_k, \qquad (4)$$

where A_{sph} is the surface area of the sphere with radius, r, onto which the binned intensities are projected. If the intersecting surface is not a sphere centered on the origin (center of the cell), then the projected area, $A_p = A \cos\theta$, must be used, where θ here is the angle between the flux propagation direction and the normal vector of the intersecting surface. Eqn. 4 implies the integrated flux at the projection plane must equal the flux incident on the cell to satisfy the conservation of energy, assuming no losses over the projection distance.

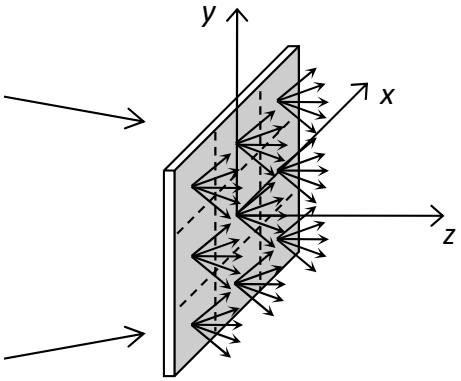

Fig. 2. Incident flux (from the left) on the target plate, and the flux re-emitting on the other side of the target. The re-emitted flux is subdivided into binned intensities at each target cell or pixel.

2.2. Angle-Binned Flux Projection Tool

After CIRCE2 bins the flux at the flat target plate, we use our flux projection tool (developed in MATLAB®) to propagate and project the binned intensities to surfaces of various shapes such as other flat plates and conical receiver surfaces like the one shown in Figure 3. This conical surface geometry is representative of real heat-absorbing receiver surfaces used in current dish-engine systems [1]. Figure 3 also illustrates the flux measured and angularly binned on a flat plate located within the receiver cavity, and then propagated to the surfaces of the conical receiver.

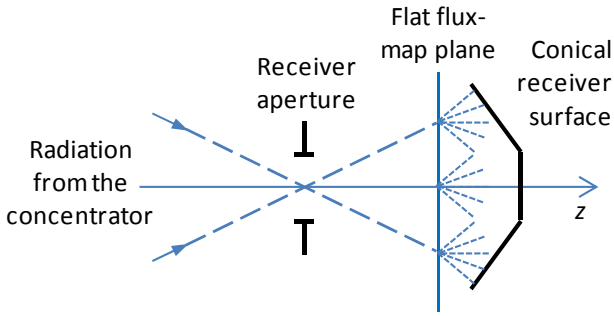

Fig. 3. A schematic of a 2-D receiver geometry for a dish concentrator, and an illustration of the incident flux on a flat plate being collected, binned, and re-projected onto the conical receiver surface. Note that the receiver is not physically in place – a mathematical model of the conical walls is generated to collect the propagated flux.

CIRCE2 outputs the angle-binned intensities to a text file. The binned intensities are separated by cell numbers and grouped into the specified polar angle bands under the cell identification. Inside the polar bands are then the intensity values at each azimuth angle band. Our flux projection tool opens the text file, and reads in and parses the data. The ordinates defined by the intersections of the polar and azimuthal angle bands are calculated for each elemental solid angle. The ordinates become the four corners that bind the solid angles as shown in Figure 4. The region inside the solid angles contains the intensity, I_{ki}. The polar and azimuth angle bands that bind the solid angle are defined by (i.e. the ordinates),

$$\Theta = [(\theta,\phi),(\theta,\phi+\Delta\phi),\ldots (\theta+\Delta\theta,\phi+\Delta\phi),(\theta+\Delta\theta,\phi)] \qquad (5)$$

The four corner points for each solid angle are stored along with the intensity value inside the solid angle bin. The four corners are then extended, or propagated, along the polar and azimuth directions to an intersecting surface, which could be a flat plane, conical, or spherical surface.

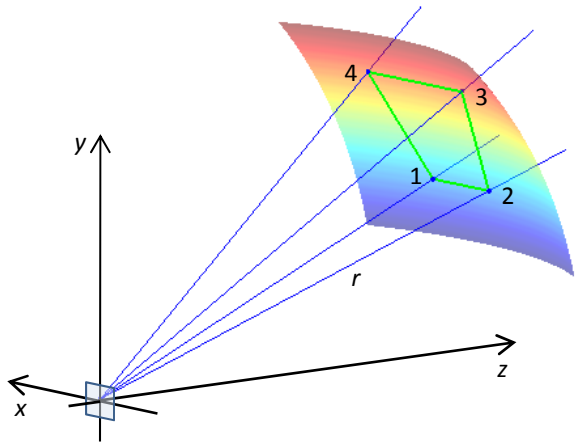

Fig. 4. Elemental solid angle bounded by the polar and azimuthal angle bands (i.e. ordinates labeled 1-4) and projected onto a sphere of radius *r*. The bounded region contains the binned intensity.

The four corner points are mapped onto the intersecting surface. The surface area of the region outlined by the four mapped points is calculated, and the mapped region is assigned the corresponding irradiance (W/m^2). This process is repeated for all the angle bins.

3. RESULTS

3.1. Projection onto flat plates

We first tried propagating and projecting the angularly binned intensities onto other flat plates perpendicular to the dish optical axis. We specify a propagation distance over which the binned intensities are propagated. The four lines shown in Figure 4 that intersect the cell center and the corners of the solid angle bin are extended and intersected with the flat plane located at some distance, *d*, along the *z* axis. This process maps the solid angle bin onto the flat plane.

A plane, in vector notation, is described by the dot product as [5]

$$\left(P - P_0\right)\cdot n = 0\,, \tag{6}$$

where n is the plane normal vector and P_0 is a point on the plane. The vector equation for a line is described by [5]

$$P(t) = L_0 + tL\,. \tag{7}$$

where L is a unit vector pointing in the direction of the line, L_0 is a point on the line, and t is a distance from L_0 along the line. Combining the plane and line vector equations provides a solution for t, or the distance to the intersections points of the line and the planar surface,

$$t = \frac{\left(P_0 - L_0\right)\cdot n}{L\cdot n}\,. \tag{8}$$

3.1.1. Mapping of solid angle bins

Using Eqn. 8, the corners of the solid angles are propagated and mapped onto a flat plane located at a distance, *d*, from the angle binning plane. Figure 5 shows the result of mapping the solid angle bins from cell *k*, for the first three polar angle bands, on to the flat plane. The corners of the mapped solid angle bins are the intersection points of the lines and the flat plane.

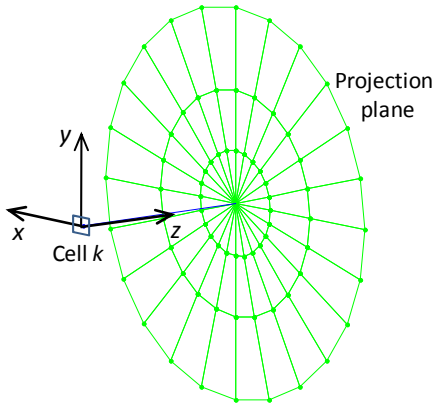

Fig. 5. Projection of the solid angle bins onto a flat plane for the first three polar angle bands of cell *k*.

The surface areas at the flat plane outlined by the mapped solid angle bins (green lines in Figure 5) are calculated, and the corresponding irradiances (W/m^2) are assigned to those surface areas. Figure 6 illustrates the mapping of two single solid angle bins of different sizes onto the projection plane located at 5.08 cm (2 in.) from the angle binning plane. The projection plane size is 0.8 m × 0.8 m on 256 × 256 pixels, so the pixels sizes are about 9.84 mm^2. The images in Figure 6 are zoomed in to better see the mapping of a single solid angle segment. In Figure 6a, the solid angle bin size is 0.070 × 0.209 radians (4° × 12°). The solid angle bin size in Figure 6b is 0.262 × 0.262 radians (15° × 15°). The white pixels correspond to the mapping (or intersection) of the solid angle bin on the projection plane. The calculated solid angle bin from the binning process is overlaid (green outlines) on the images to see its mapping onto the projection plane.

Two effects can be seen in Figure 6. The first is the pixilation effect. Since the pixels are square and of finite size, they cannot completely and perfectly fill the area bounded by the green outline. This effect leaves small voids in the bounded region. Conversely, some pixels also "leak" or extend into the neighboring solid angle bins. The pixels that "leak" out can potentially cause problems by combining with "leaking" pixels from other solid angle bins. An accumulation of these pixels can cause hot spots on the final flux profile. The combined effect of the voids and pixel "leakage" typically causes streaks

and speckle in the final flux profile. One solution we considered is to shrink the pixel size (i.e. increase the pixel density). This of course is at the expense of longer processing times. With the target plane size at 256 × 256 pixels, this effect is not very prevalent.

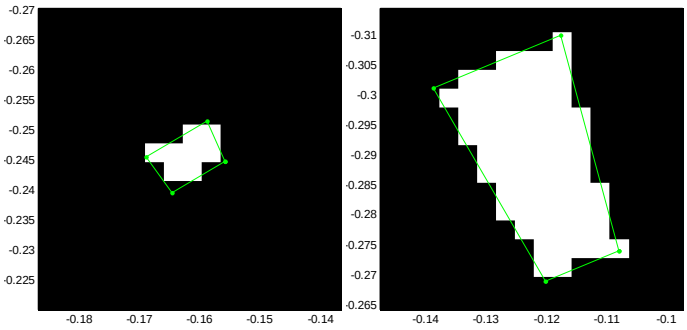

(a) (b)

Fig. 6. Mapping of a (a) small solid angle bin and (b) large solid angle bin onto the projection target plane.

The second effect is caused by the difference between the mapped area (in pixels) and the actual area of the solid angle bin on the projection plane. This is also due to pixilation, but the error from the difference in the areas can cause bigger errors. The actual solid angle bin (green outline) carries the correct magnitude of the intensity. When mapped onto the projection plane, the surface area of the green outline must be used to get the correct irradiance distributed on the group of intersecting pixels. If, however, the area from the pixels is used, the mapped irradiance will be incorrect. For example, if the area from the pixels is smaller than the green outline, there will be an artificial increase in the irradiance being mapped onto the projection plane. Slight increases in irradiances from other solid angle bins will result in a higher irradiance in the final flux profile. In Table 1, we show the difference in the mapped areas for the cases shown in Figure 6. When the solid angle bins are smaller, the difference between the area from the intersected pixels and the actual mapped area (green outline) is bigger. There are two solutions we considered to minimize the error: 1) increase the pixel density at the target projection plane (i.e. decrease the pixels size), but this is at the expense of longer processing times, and 2) increase the size of the solid angle bins, but this will reduce the sampling resolution. The solution that we currently use is to calculate the mapped area from the green outline, and use that calculation to determine the irradiance contained in that solid angle. We then distribute the irradiance evenly over the intersected pixels. This is easy to do for flat projection planes, but can be difficult for curved projection surfaces. This issue surrounding conical surfaces will be discussed in Section 3.2.

Perhaps a better solution might be, once the projected area of the solid angle is mapped, to correctly ratio the irradiance between the pixels shared by neighboring solid angle bins, instead of spreading the irradiance evenly over all the intersected pixels. With this approach we can keep the receiving plane frame size to 256 × 256 pixels and the number of solid angle bins high for good sampling of the flux. The development of this approach is proposed for future work

Table 1. Differences in the mapped areas (reference to Fig. 6).

	Mapped area of the green outline (mm^2)	Mapped area using pixels (mm^2)	% Error
Small angle bin (4° × 12°)	80.725	78.739	2.5
Large angle bin (15° × 15°)	667.919	669.281	0.2

We showed the mapping of a single solid angle bin from a single cell, discussed the issues with the mapping process, and offered solutions to the issues. The mapping of the solid angle bins and the corresponding irradiance happens many times in a single run. If errors exist in the mapping process, they will accumulate quickly. For example, for the case of Figure 6a, the flux is angularly binned on a 201 × 201 point grid; the polar angles are divided into 15 segments, and the azimuth angles are divided into 30 segments. Over 18 million (201×201×15×30) solid angle bins are then generated and mapped. However, most of the solid angle bins carry zero intensity. This reduces the number of solid angles bins to 20-30% of the total. By removing the solid angle bins that carry zero intensity, we also significantly reduce the processing time. In Figure 7, we show the mapping of three solid angle bins, one each from three consecutive cells, and the accumulation of the irradiance values where the solid angle bins overlap. The solid angle sizes are the same as the ones shown in Figure 6.

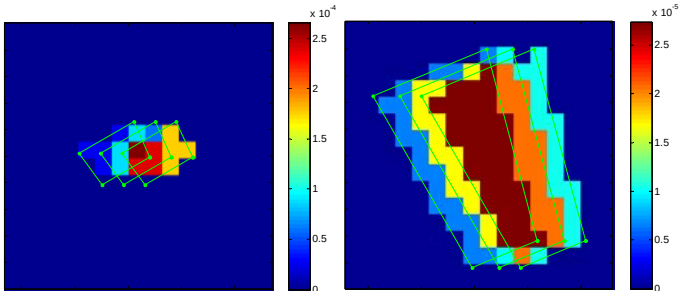

(a) (b)

Fig. 7. Illustration of solid angle bin mapping and accumulation of the irradiances in the overlap regions for (a) small solid angle bins and (b) large solid angle bins.

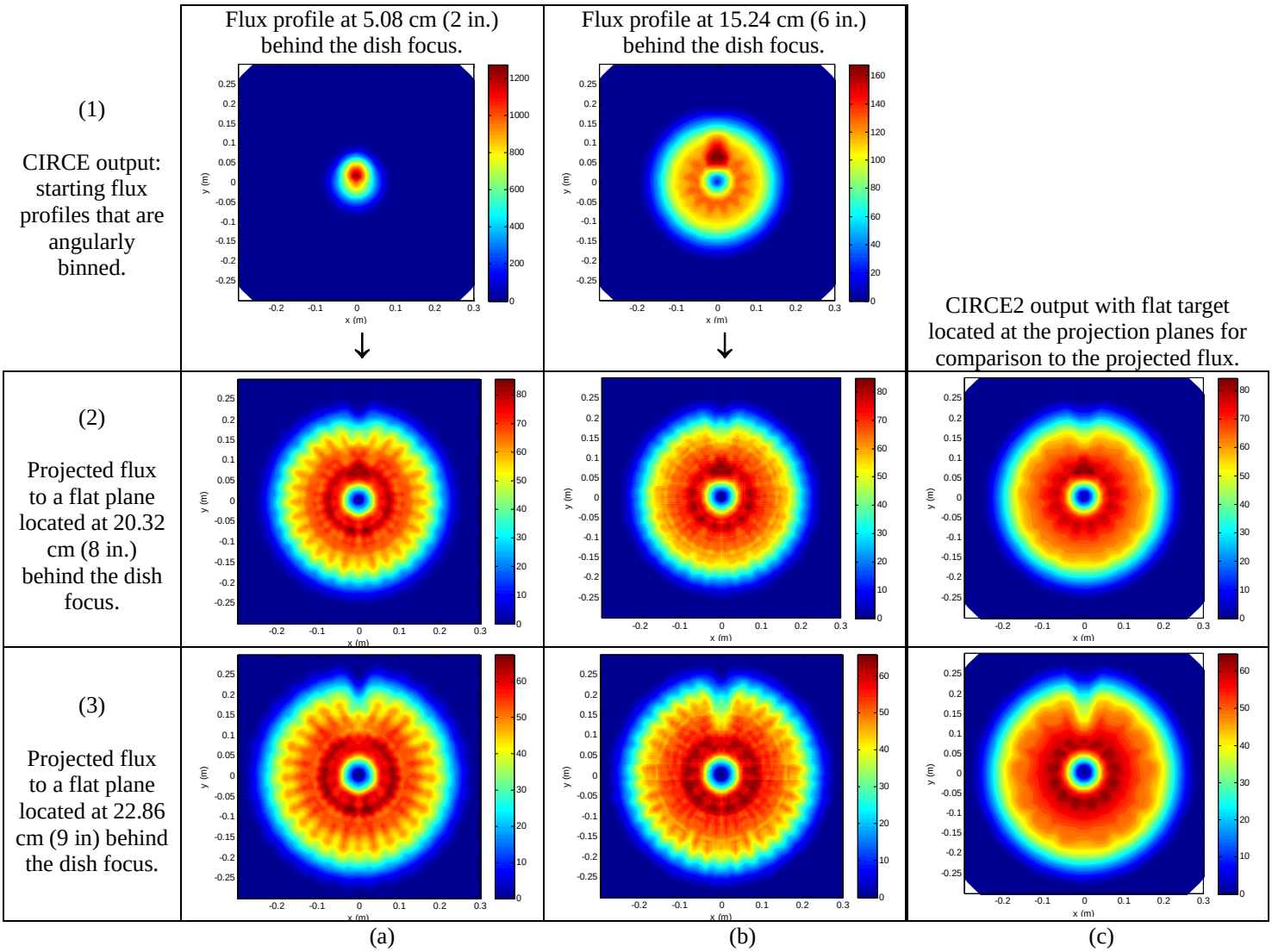

Fig. 8. Examples of flux projection onto flat planes from two different starting flux profiles (1a) and (1b), and a comparison to CIRCE2 output at the same projection planes (c). The units between the projected flux and the CIRCE2 output are consistent. The notches at the top of the flux images correspond to the gap (i.e. missing facets) typical in dish concentrators to allow the boom that holds the engine to be extended out from the support structure.

Table 2. Flux angle binning parameters for the starting flux profiles shown in Figure 8-1a,1b.

Starting flux profile	Target size (m^2)	Number of target grid points	Polar angle range (rad)	Polar angle bin size (rad)	Azimuth angle bin size (rad)
5.08 cm from the dish focus (Fig. 8-1a)	0.4 × 0.4	101 × 101	0 - π/3 (0 – 60°)	π/45 (4°)	π/15 (12°)
15.24 cm from the dish focus (Fig. 8-1b)	0.4 × 0.4	201 × 201	0 - π/3 (0 – 60°)	π/45 (4°)	π/18 (10°)

3.1.2. Flux projection results

CIRCE2 was set up to output the flux distribution profiles at locations 5.08 cm (2 in.) and 15.24 cm (6 in.) behind the model dish focus (Figure 8, row 1). The flux at 5.08 cm from focus was sampled on a 101 × 101 point grid, and the flux at 15.24 cm from focus was sampled on a 201 × 201 point grid. For both cases, the polar angle range was limited to 0 to π/3 radians (0 to 60°). The polar angle was divided into 15 equal angle segments. The azimuth angle was divided into 30 and 36

equal angle segments for the flux at 5.08 cm and 15.24 cm, respectively. These binning parameters are repeated in Table 2.

The top row of images in Figure 8 (row 1) shows the starting flux profiles, which are angularly binned. The corresponding projected fluxes are shown directly below. Also shown in the right column (Figure 8c) are the CIRCE2 flux profiles at the same projected flux plane locations for comparison to the projected flux.

The two starting flux profiles were propagated to flat target planes 0.8 m × 0.8 m (256×256 pixels) in size located at 20.32 cm (8 in.) and 22.86 cm (9 in.) behind the dish focus. The projection distances for the first case (Figure 8a) are then 15.24 cm (6 in.) and 17.78 cm (7 in.). The projection distances for the second case (Figure 8b) are 5.08 cm (2 in.) and 7.62 cm (3 in.). Rows 2 and 3 in Figure 8 (directly below the starting flux images) show the results of the flux projection. The images are cropped to -0.3 m to 0.3 m. For comparison, CIRCE2 was re-run with flat targets at the same locations as the projection planes (Figure 8c).

By comparing the projected fluxes in rows 2 and 3 in Figure 8 to the CIRCE2 output (Figure 8c), we see that the projected fluxes show that same character as the CIRCE2 output. The flux scaling is on the same order of magnitude, and the peak fluxes agree to within 1% of the CIRCE2 output.

The differences between the long (Fig. 8a) and short (Fig. 8b) distance flux projections, however, are noticeable. In the case of the short distance flux projection, the solid angle bins were smaller. Since the projection distances were relatively short, the solid angle bins did not grow much over the short distance, and so the mapped areas were small. The pixilation effect (i.e. streaks) described above can be seen in the images (Figure 8b). In the case of the long projection distances, the solid angle bins were also small, but since they were projected over longer distances, they grew and thus mapped to larger areas on the projection plane. The pixilation effect was reduced in this case (Figure 8a).

There is an additional artifact that can be seen in the projected fluxes. There is petal-like formation around the edges of the flux pattern at about the 60% zone that is not seen in the CIRCE2 flux profiles. These are more pronounced for longer projection distances. There seems to be some correlation between the number of petals around the flux pattern and the number of azimuth angle bins, although they do not match in number exactly. As the number of azimuth angle bins is reduced, so do the number of petals. To reduce the petaling effect, the azimuth angle bins can be made large, but again this is at the expense of the sampling resolution. We currently do not have a solution to reduce the petaling effect without decreasing the sampling resolution.

3.2. Projection onto conical surfaces

The next step was to project the binned intensities onto a conical surface like the one shown in Figure 3. Instead of a flat projection plane, we now define a conical projection surface. A three-dimensional conical surface in vector notation is defined by a dot product as [6]

$$A \cdot \left(\frac{P - V}{|P - V|} \right) = \cos \alpha \,, \tag{9}$$

where A is the direction vector of the cone (pointing from the cone vertex towards the opening), V is the vertex location, P is a point on the cone surface, and α is half the apex angle of the cone. Eqn. 9 is typically squared and rearranged to get the following quadratic equation,

$$(P - V)^T M (P - V) = 0 \,, \tag{10}$$

where $M = \left(AA^T - \cos^2 \alpha \cdot I \right)$. $(.)^T$ symbolizes a matrix transpose, and 'I' is the identity matrix. The line equation (Eqn. 7) can be substituted into Eqn. 10 and the intersection points of the line at the cone surfaces can be determined. The quadratic equation will produce two solutions. This is because Eqn. 9 forms two cones; the main cone and its reflection at the vertex. The line then intersects both cones to produce two intersection points or two solutions. To restrict Eqn. 9 to the main cone of interest, we apply the condition,

$$A \cdot (P - V) \geq 0 \,. \tag{11}$$

We then use Eqns. 10 and 11 to model the conical shape of the receiver. The tilted planes that form the cone (in Figure 3) are virtually extended and intersected with the dish axis to locate the cone vertex, V. The vector A points in the *–z* direction, and P becomes the line intersection points on the cone surface. The angle, α, is calculated from the receiver design geometry.

Similar to the flat plane projections, a flux profile is generated with CIRCE2 on a flat target located between the dish focus and the receiver surface. The flux on the flat target is angularly binned, and the binned fluxes are then projected onto the conical surface.

The lines that originate from the center of the cell through the four corners of the elemental solid angles are now intersected with the conical surface. The mapped corner points form a trapezoidal shape on the conical surface for which the surface area is then calculated. In this case, since the cone surface is tilted, the projected areas ($A_p = A \cos\theta$,) must be used. Figure 9 illustrates the mapping of the solid angles bins from the center cell of the target grid onto a conical surface. The irradiance (W/m^2) is assigned to the pixels that are intersected by projected area.

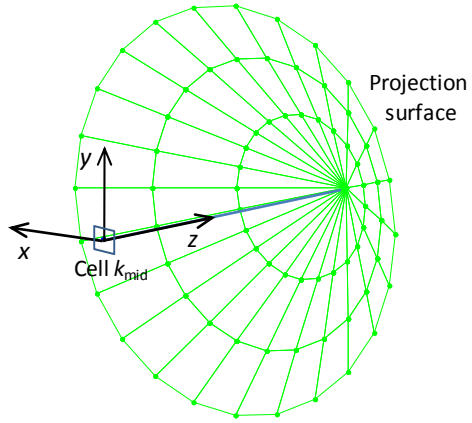

Fig. 9. Projection of the solid angle bins onto a conical surface for the first three polar bands.

In addition to the issues described for projections onto flat planes, cone surface projections carry an additional issue. Since only the four corner points of the solid angle bins are projected and intersected with the cone surface, we can only form a plane at the cone surface between the four points. We can easily calculate the area of this trapezoidal plane, but what we need is the surface area on the curved cone surface. If we use the area of the plane, then we are underestimating the surface area, which results in artificially increasing the irradiance contained in the solid angle bin. We considered two possible solutions: 1) we can add more points to the solid angle bins, or 2) we can make the solid angle bins as small as possible. In the first solution, we can add more points, in addition to the corner points, to the solid angle bin. More points can then be intersected with the cone and a better estimate of the intersected surface area can be calculated. This, however, adds more data points to the already large data sets, and we become limited by the memory and processing speed of the computer. Perhaps by batching the data sets we can overcome the limitations. In the second solution, smaller solid angle bins map to smaller trapezoidal areas on the cone surface, where the difference between the areas of the trapezoidal planes and the intersected surface areas become negligible. But again smaller solid angle bins implies more solid angle bins and larger data sets. The solution we currently use is to keep the solid angle bins to moderate sizes and determine coefficients that become scaling factors to the calculated plane trapezoidal areas so the result is closer to the intersected surface areas. We do this by comparing the projected fluxmap to the CIRCE2 output. We compare the flux values at a few different points on the fluxmaps, we adjust the scaling coefficients, and re-project the binned fluxes. We iterate until the flux values at the different points between the projected fluxmap and the CIRCE2 output agree to within 1%. For now this solution provides good results. In the future one of the two solutions proposed may be implemented. Yet a better solution would be to calculate the theoretical intersected surface areas, but this is not easy for highly irregular trapezoids that get mapped (especially from the corner cells) onto the cone surface.

3.2.1. Flux projection results

Figure 10a,b shows examples of the angularly binned flux projected onto a conical receiver surface. The center portion of the receiver is called the plug which is modeled with a cone segment with a flat top. The same binning parameters given in Table 2 were used. For comparison, CIRCE2 was re-run with the same receiver geometry used in the flux projections (Figure 10c).

The projected fluxes show the same general character as the CIRCE2 output. The flux levels for both the projected flux and the CIRCE2 output were of the same magnitude. The peak fluxes agreed to within 1%. Some petaling effect can be seen the Figure 10a due to the longer projection distance. In Figure 10b, streaks caused by the pixilation effect can be seen.

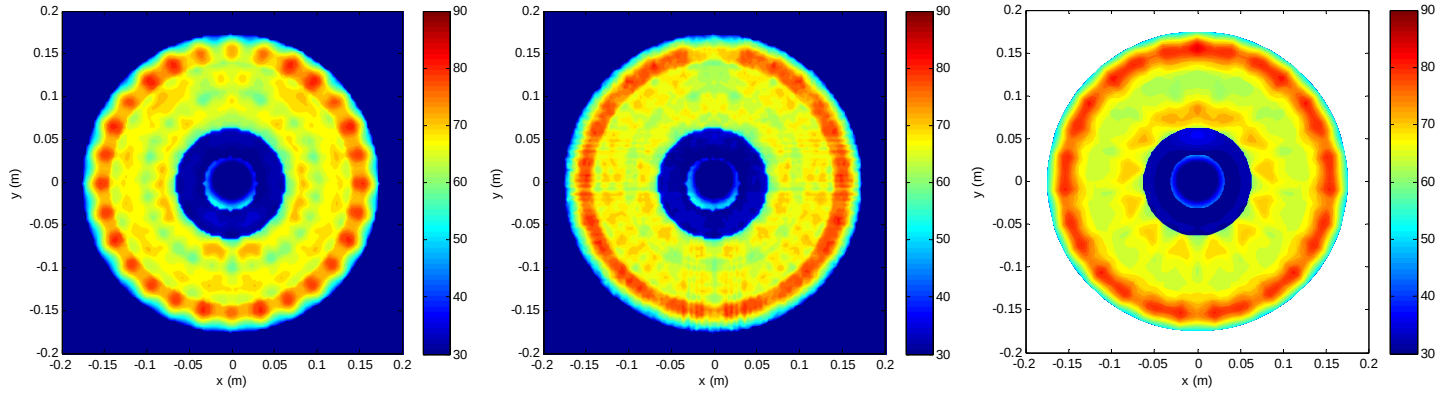

(a) (b) (c)

Fig. 10. Flux profiles on a conical dish receiver similar to the type shown in Figure 3. Flux projection onto a conical receiver surface over a (a) long and (b) short projection distance, and (c) a CIRCE2 output using a receiver of the same geometry for comparison. The center portion of the receiver is the receiver plug.

3.3. Projection of real flat plate measured flux

Ultimately, the goal for our flux projection tool is to take real measured flux profiles obtained with the flux-mapper (beam characterization system or BCS), angularly bin the flux, and project the binned flux onto non-flat receiver geometries. In a real fluxmap measurement for a dish-engine system, the dish engine package is first removed and replaced with a flux-mapper or the BCS. The flux-mapper consists of a flat water-cooled Lambertian target and a digital camera that looks at the target and collects images of the flux profile on the target. The target is mounted on rails that allow the target to move along dish optical axis. Typically images of flux profiles are collected in the vicinity of the dish focus and the heat coils (receiver) location.

For the flux projection process to work, the flux images collected with the flux-mapper must be properly binned into elemental solid angles. We do not have the benefit of automatically performing the angle binning on the flux images as we did with the CIRCE2 models. Our approach is to model the dish concentrator reasonably well in CIRCE2, generate the flux profiles at the ideal location, and angularly bin the flux. We then use the flux-mapper to collect real flux profiles from the dish concentrator at the same location as in the CIRCE2 run. We can match the measured flux profile to the CIRCE2 output, and then update the flux values contained in the solid angle bins with the values from the real flux-map.

Figure 11a shows an example of a flux profile from a dish concentrator collected with the flux-mapper. This particular flux is collected at a location 15.24 cm (6 in.) behind the dish focus, similar to the CIRCE2 model in Figure 8-1b. Two fiducials on the flux-mapper target (visible in Figure 11a) that are 76.2 cm (3 in.) apart are used to correctly scale the dimensions of the flux image. We then re-sample the flux image using a two-dimensional spline interpolation and crop the image to match it to the CIRCE2 fluxmap. To match the scaling of the pixel values, both fluxmaps (flux-mapper image and CIRCE2 fluxmap) are integrated, and a scaling factor is determined from the ratio of the integrated values. The scaling factor is then applied to the flux-mapper image. With the flux-mapper image now properly matched to the CIRCE2 fluxmap, we replace the flux values in the solid angle bins with the values from the flux-mapper image. From here, the projection process is the same as previously described.

Figure 11b is a projection of the flux image in Figure 11a to a flat plane. The projection distance is 5.08 cm (2 in.). The flux image in Figure 11c was collected with the flux-mapper at the same location as the projection plane; we show it for comparison to the projected flux image. The general character of the flux profiles is similar. The major features (e.g. bulge on the lower right) were carried through during the projection. Since the projection distance was short, streaking due to pixilation is visible in the projected flux image.

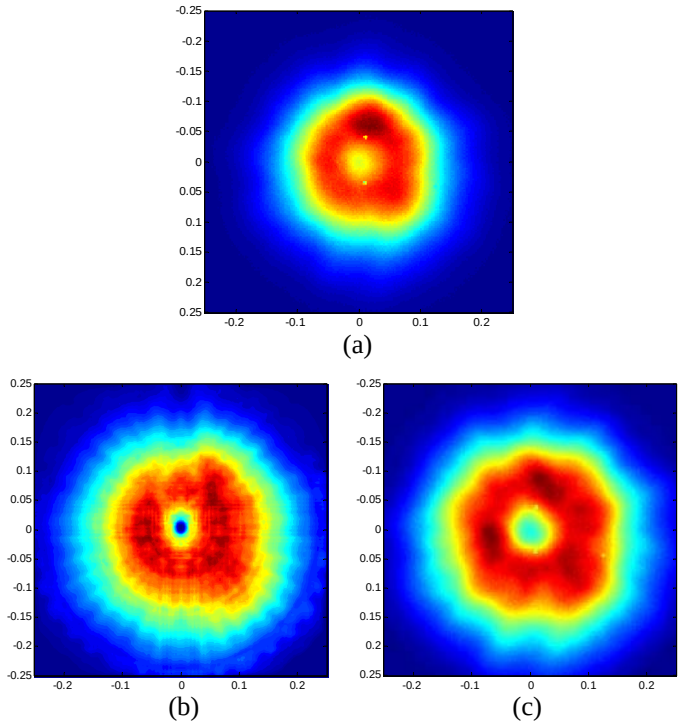

Fig. 11. Example of a projection of real measured flux. The flux image in (a) is the starting flux, (b) is the projected flux, and (c) is for comparison to the projected flux image.

Figure 12 shows a projection of the measured flux in Figure 11a onto the same conical receiver model used before. The *z* scale (colorbar) is matched to the results shown in Figure 10 for comparison. The result shows that there is higher flux on the right side of the receiver, which could cause an imbalance on the four coil bundles arranged on four quadrants [4]. This typically leads to a reduction in efficiency of the engine. In addition, more flux is appearing on the receiver center plug, which is typically not desired. The dish and/or the individual facets would then need to be adjusted to improve the flux distributions on the receiver.

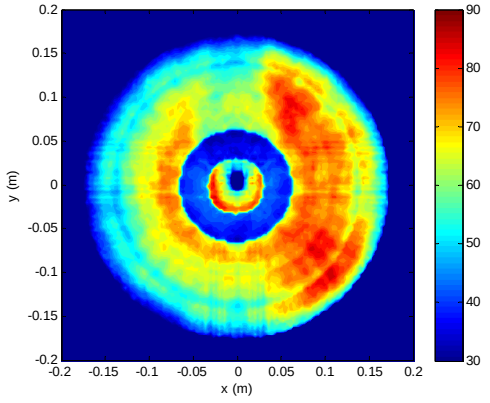

Fig. 12. Projection of a real measured flux onto a conical receiver.

4. CONCLUSION AND FUTURE WORK

Radiosity limits the flux to be measured to flat surfaces. Dish-engine system receivers, however, are typically non-flat. Potential problems such as hot spots or flux imbalance on the receiver heat-absorbing coils drive the need to evaluate flux distributions on the coils. But flux profiles on non-flat geometries cannot easily be obtained directly. Typically the flux profiles on the non-flat geometries are inferred from multiple flat plate measurements in the vicinity of the receiver coils. This approach is not ideal and can lead to improper evaluation of flux distributions on the receiver coils.

We proposed a method that projects flat target flux profiles to non-flat receiver surface geometries. We modeled a dish concentrator in CIRCE2 and obtained flux profiles at locations between the dish focus and the receiver surface. We used CIRCE2's angular flux binning feature to subdivide the incident flux on the flat plate into elemental solid angle bins, and then analytically project flux intensities contained in the solid angle bins to other flat surfaces and conical surfaces. We compared our projected flux results to flux profiles directly output from CIRCE2. Our projected flux agreed very well with the CIRCE2 output. The character of the fluxmaps was maintained, and the peak fluxes agreed to within 1%. After verifying the projection tool works reasonably well with CIRCE2 models, we attempted to project real measured flux onto a flat plane and then onto a conical receiver geometry.

Our flux projection tool works reasonably well, but is still not perfect. We identified issues with short distance projections. Flux "leakage" causes pixilation effects in the projected flux images. This effect is minimal in longer projection distances. But petaling around the flux pattern appear in long projection distances. We proposed solutions for these various issues described. For future developmental work, we plan to implement some of the proposed solutions to improve the tool.

ACKNOWLEDGMENTS

Sandia National Laboratories is a multi-program laboratory managed and operated by Sandia Corporation, a wholly owned subsidiary of Lockheed Martin Corporation, for the U.S. Department of Energy's National Nuclear Security Administration under contract DE-AC04-94AL85000. The United States Government retains and the publisher, by accepting the article for publication, acknowledges that the United States Government retains a non-exclusive, paid-up, irrevocable, world-wide license to publish or reproduce the published form of this manuscript, or allow others to do so, for United States Government purposes.

REFERENCES

[1] Andraka, C.E., Yellowhair, J, Iverson, B.D., (2009, May). A parametric study of the impact of various error contributions on the flux distribution of a solar dish concentrator. *Proceedings of the ASME 2010 4th International Conference on Energy Sustainability, Phoenix AZ USA.*

[2] Khalsa, S.S, & Ho, C.K., (2010, September). Development of rigorous boundary conditions to simulate receiver irradiance from heliostat fields and dish concentrators. *Proceedings of the SolarPACES Conference, Perpignan, France*.

[3] Romero, V. J. (1991). *CIRCE2/DEKGEN2: A Software Package for Facilitated Optical Analysis of 3-D Distributed Solar Energy Concentrators – Theory and User Manual* (SAND91-2238). Sandia National Laboratories, Albuquerque, NM.

[4] Romero, V. J. (1994, July 29). *ANGFLUX/ANGDEK, a special version of the CIRCE2/DEKGEN2 solar concentrator modeling package*. Memo to D. R. Gallup at Sandia National Laboratories, Albuquerque, NM.

[5] *Line-plane intersection* (2011). Retrieved from http://en.wikipedia.org/wiki/Line-plane_intersection

[6] Eberly, D. (2008). *Intersection of a line and a cone*. Retrieved from http://www.geometricals.com/Lib Mathematics/Intersection/Intersection.html

